Available online at www.sciencedirect.com
ScienceDirect
Journal of the European Ceramic Society 29 (2009) 2469–2479
www.elsevier.com/locate/jeurceramsoc

Sintering of glass matrix composites with small rigid inclusions

Markus Eberstein [a,*,1], Stefan Reinsch [a], Ralf Müller [a], Joachim Deubener [b], Wolfgang A. Schiller [a]

[a] *BAM Federal Institute for Materials Research and Testing, 12203 Berlin, Germany*
[b] *Institute of Non-Metallic Materials, Technical University Clausthal, 38678 Clausthal-Zellerfeld, Germany*

Received 17 May 2008; received in revised form 30 January 2009; accepted 17 February 2009
Available online 1 April 2009

Abstract

We investigated the effect of dispersed crystalline particle volume content Φ on sintering of glass matrix composites (GMC) for low-temperature co-fired ceramics (LTCC) applications. Such composites typically consist of alumo-borosilicate glass and α-Al_2O_3 powders of similar average particle size ($D_{50} \approx 3\,\mu m$). Sintering shrinkage was observed by dilatometry and heating microscopy and was backed up by glass viscosity measurements. Microstructure analysis revealed that α-Al_2O_3 particles do neither show significant dissolution into the liquid phase nor detectable crystallization throughout LTCC firing schedules. Therefore, in this study α-Al_2O_3 particles were treated as small rigid inclusions. It was found that Φ lowers the shrinkage rate of GMC. While the lowering is small for small Φ and at the early stage of densification it progressively increases during sintering, and final shrinkage shifts up to 170 K to higher temperatures for $\Phi = 0.45$. The behaviour observed could be explained assuming that sintering is controlled by the effective viscosity, which progressively increases non-linearly during densification due to the gradually wetting of the surface area of corundum particles. We could demonstrate that Al_2O_3 cluster can cause residual pores and reduce the attainable shrinkage. The reduction of attainable shrinkage is found to depend on Φ^3, reaching about 8% at $\Phi = 0.45$.

Keywords: Glass ceramics; Inclusions; Sintering; Mixing; Powders, solid-state reaction

1. Introduction

Manifold ceramic applications, like sealings, coatings, reinforced glasses and enamels take advantage of glass matrix composites (GMC). GMC are made by powder processing and sintering of glass powders containing certain amounts of dispersed crystalline particles. Microstructure and properties of these materials can be widely tailored by selection of appropriate glass and crystal powders, volume fractions, powder processing and firing schedule.

GMC typically sinter below 900 °C favoring those materials for chip packaging technology as low-temperature co-fired ceramics (LTCC).[1,2] LTCC enable the integration of wiring, passive components, mechanical, and fluidic functions in compact 3D architectures formed by co-firing of silver conductors (melting point 961 °C) and other components inside stacked ceramic tapes. In contrast to conventional polymer materials, LTCC-multilayer provide, e.g. enhanced mechanical and thermal stability, impermeability for gases and water as well as long-life reliability. These specific advantages have lead to a progressive use of LTCC in automotive, medicine and telecommunication engineering.

To match process and product property demands, LTCC are usually composed of glass and crystalline powders of similar small particle size ($D_{97} < 3\,\mu m$), which often results in complex dissolution and crystallization phenomena during sintering. Thus, various effects as the influence of glass and crystalline particle size distribution, the impact of rigid crystalline inclusions on the effective viscous flow of the composite, partial dissolution of the dispersed crystalline particles into the liquid phase and related consequences on its composition, viscosity and crystallization behaviour as well as manifold mutual interactions have to be controlled during firing.

Appropriate control can benefit from numerous excellent papers on sintering of glass powders[3] particular with respect to the onset[4] and the final state of sintering.[5] While in these papers

* Corresponding author. Tel.: +49 6181 35 9157; fax: +49 6181 35 4450.
E-mail address: markus.eberstein@heraeus.com (M. Eberstein).
[1] Now with W.C. Heraeus GmbH, Thick Film Materials Division, Business Unit TH, Heraeusstr. 12-14, D-63450 Hanau, Germany.

0955-2219/$ – see front matter © 2009 Elsevier Ltd. All rights reserved.
doi:10.1016/j.jeurceramsoc.2009.02.007

special geometric conditions are assumed, others follow more general stereological[6] or rheological[7] concepts. Many specific problems have been addressed including the sintering of nano-sized particles,[8–11] the effect of bi-[12] and polydispersed particle size distribution,[13] the effect of sintering anisotropy[14,15] as well as concurrent crystallization.[16] Numerous papers focus on sintering of GMC concerning various applicative aspects,[17–22] the effect of rigid inclusions on the effective composite viscosity,[23] sinter anisotropy,[24] sinter retardation,[25–27] as well as the coexistence of solid and liquid phases.[28–32] Recently, sinter-forging or loading dilatometry studies on LTCC were focused on the anisotropic constrained sintering characteristics and microstructure of LTCC[33–36] analyzing respective viscous properties and sintering stress. The macroscopic description of constrained sintering was based on the concept of the viscoelastic analogy[37,38] and related constitutive models.[39–44] This theoretical framework and related experimental data were utilized to simulate sintering[45] and bilayered structures.[46] Comprehensive reviews are presented in Refs. [47,48].

However, most of these sinter kinetic studies are restricted to special limitations of powder morphology and composition and cannot be formally adopted regardless of the particularities of the given LTCC composition without appropriate adjustment. For this reason, LTCC materials development is still mainly based on empirical experiences.

The aim of the present paper is to study the influence of rigid inclusions similar in average size to that of the glass powder on sintering. Accordingly, we have chosen model GMC containing up to 45 vol.% of α-Al_2O_3 particles immersed in a alumo-borosilicate glass matrix which does not show noteworthy dissolution of crystal particles into the glass and glass crystallization throughout typical LTCC time–temperature schedules. Sintering was studied during heating with 5 K/min by dilatometry and heating microscopy, backed up by glass viscosity measurements, powder and powder compact characterization and microstructure analysis. Special attention is drawn to the accurate measurement of basic properties important for understanding and kinetic modeling of GMC shrinkage. This modeling and the effective GMC viscosity required has been partially discussed in Ref. [49] and will be addressed in separate papers.

2. Experimental procedure

2.1. Preparation

2.1.1. Glass

A glass batch of 2500 g was inductively melted in a 4 l Pt crucible at 1600 °C for 3 h. Homogenization of the melt was endorsed by stirring for 1 h. The glass melt was then casted on a steel plate and the resulting bulk glass was subsequently quenched in water. The batch composition and chemical analysis of the glass are given in Table 1. All experiments refer to powders made from this batch to ensure compositional homogeneity.

2.1.2. Powders

Powder preparation was carried out by several steps according to LTCC technology. First, glass pieces were exposed to crushing (BB51, Retsch, equipped with ZrO_2-plates). Subsequent vibration-ball milling (LS 60/Liebe) was applied to attain the required input median diameter $D_{50} < 50\,\mu m$ for attritor milling (PE 075, Netzsch), by which the final particle size ($D_{50} \approx 3\,\mu m$ and $D_{50} \approx 5\,\mu m$) was tuned. We used alcohol as milling dispersant, which was removed by a rotation-evaporator (Rotavapor E-131, Büchi) afterwards. The milling progress was monitored by particle size analysis of probed powder samples. For fabrication of GMC the glass was mixed with up to 45 vol.% of α-Al_2O_3 (Martinswerk MDS 6, $D_{50} \approx 6\,\mu m$, density 3.96 g cm^{-3}; volume contents $\Phi = 0.05$, 0.15, 0.25, 0.35, 0.45). In order to obtain uniform particle size distribution (PSD) for both glass and corundum particles as well as to achieve good mixing, the desired fraction of α-Al_2O_3 was added when the median particle size of the glass particles equaled that of the corundum powder. Afterwards, the mixture was exposed to a final mix-milling step.

Table 1
Chemical composition of the used alumo-borosilicate glass by batch and by XRF analysis. The deviation to 100% in the analysis data is due to the uncertainty of the analysis procedure.

	mol%	wt.% batch	wt.% analysis
SiO_2	63.6	50.0	49.1
B_2O_3	15.4	14.0	12.5
BaO	12.0	24.0	22.8
Al_2O_3	9.0	12.0	11.7

2.1.3. Powder compacts

Powder compacts of cylindrical shape were made by uniaxial pressing (60 MPa, $\emptyset = 8$ mm, h = 5–8 mm). Cuboids were pressed for horizontal dilatometry (5 mm × 5 mm × 15 mm). We used Uniox 20000 (Nippon Oil & Fats Co., Ltd.) as a pressing aid. It could be added to the milling slurry since it remains on the surface of the particles after removing of the alcohol. Debindering of pressed compacts was achieved by heating at 2 K/min to 600 °C in air.

2.1.4. Microscopy and XRD samples

For investigation of the evolution of the microstructure during sintering at 5 K/min, powder compacts were accordingly heated to selected temperatures and quenched in air. This annealing was carried out in an electric furnace (Linn Electro Therm, tube furnace FRH-20/150/1100). Annealed specimens were embedded in resin, grinded and polished afterwards. The cross-section was observed by an environmental scanning electron microscope (ESEM-FEG, Philips-XL 30, Eindhoven).

2.2. Glass properties and GMC sintering

2.2.1. Glass viscosity

The glass viscosity was determined by complementary methods. T_g was determined by a horizontal dilatometer (Netzsch 404 E, $\Delta T_g \approx \pm 3$ K). Bending beam viscometry was utilized for the range $\eta = 10^{12.3}$ to 10^9 Pa s (Bähr VIS 401, $\Delta \log \eta \approx \pm 0.15$). In the range $\eta = 10^9$ to 10^7 Pa s, Parallel

Plate viscometry (Bähr VIS 404, $\Delta\log\eta \approx \pm 0.15$) and for $\eta < 10^5$ Pa s ($T > 1000\,^{\circ}$C) concentric cylinder viscometry (Haake VT550/BAM, $\Delta\log\eta \approx \pm 0.1$) was applied. Heating microscopy was used to determine characteristic viscosity fixed points of powder compacts (sinter onset point: $\eta = 10^{8.6}$, final sinter point $\eta = 10^{6.8}$ Pa s, minimal point: $\eta = 10^{4.4}$ Pa s, hemisphere point: $\eta = 10^{2.8}$ Pa s, flow point: $\eta = 10^{2.0}$ Pa s).

2.2.2. Glass density

Glass density was measured from powders <40 μm by means of a pycnometer (Accupyc 133 V.1.03, He, $\Delta\rho \approx \pm 0.001$ g cm^{-3}).

2.2.3. Particle size

The particle size distribution of all obtained powders was measured by laser diffraction (He–Ne laser, $\lambda = 633$ nm, Mastersizer S, Malvern Instruments GmbH). This method was also applied for monitoring the milling progress by using sampled powders.

2.2.4. Compact density

Bulk density of green and sintered specimens was obtained from sample geometry (measuring or heating microscope) and weight. Relative density was calculated from the ratio of bulk density to theoretical density. Theoretical density was obtained from the volume ratio and single densities of glass and alumina. In some cases, sintered specimens were grinded, polished and the cross-section was imaged by a visible light microscope (12× objective) to detect and quantify porosity using the software Image C/a4i (Image C, aquinto AG). The software was also applied to selected ESEM pictures in order to determine amount and distribution of crystalline particles in dense sintered specimens. Errors in volume amount measurement depend on operator and were estimated to be lower than 2% for this work.

2.2.5. Sintering

Shrinkage of cylindrical powder compacts was measured at 5 K/min by different methods. First we used vertical dilatometry (Linseis L70/BAM). The load applied by the sample holder varied from 1 to 3 cN; respective pressures on the sample were from 0.2 to 0.6 kPa for 50.3 mm^2 sample diameter. Furthermore, a horizontal dilatometer (802-S Bähr) was used. Load applied was 4 cN; respective pressure on the sample was 1.6 kPa (4 cN per 25 mm^2 frontal area). Finally, heating microscopy image analysis was used. To investigate precision and reproducibility of this method, measurements were done by two devices, a semi-automated one at BAM (Leitz Heating Microscope, Novocontrol temperature controller), and a fully automated one at TU Clausthal (Hesse Instruments, Osterode, Germany). Both devices are equipped with optical data acquisition and image analysis allowing to measure axial and radial strain. The accuracy of optical detection of sample geometry changes corresponds to a shrinkage error of ±0.1%.

Sample temperature was measured at different positions and did not deviate more than about 5 K. Nevertheless, non-homogeneous temperature distribution within the powder compact can influence sintering. This effect should be most pronounced at low temperature for the non-isothermal sintering considered here. Thus, with increasing temperature, heat transfer is accelerated due to decreasing porosity as well as to the increased contribution of heat radiation. We estimate that the maximum temperature deviation between the sample surface and the interior is in the order of 10 K. This estimation is based on temperature gradient measurements reported in Ref. [13], where powder compacts similar in size to the present case were exposed to temperature steps of ≈200 K and reached thermal equilibrium within ≈100 s.

2.2.6. Crystallization

To detect the onset of crystallization during sintering at 5 K/min, powder samples were studied by means of DTA (TAG 24 Setaram, sample weight 25 mg). Differently annealed powder compacts, prepared as described in Section 3.1, were studied by XRD (Philips PW 1710 Cu Kα).

3. Results

3.1. Glass properties

Newtonian viscosity η was determined in the range from $10^{12.30}$ to $10^{1.93}$ Pa s. The temperature dependence was analysed using a Vogel–Fulcher–Tammann (VFT) equation. Log η is best fitted by $\log\eta = -4.27 + 7487/(T - 202)$ (in units of Pa s and °C, solid line of Fig. 1). Important for investigation and kinetic modeling of shrinkage of LTCC-GMC is the viscosity in the temperature range 750–900 °C (see Figs. 8 and 9), about 100 K above glass transition temperature T_g. In this range, the viscosity is often interpolated between T_g and viscosity data obtained from concentric cylinder experiments as emphasized in Fig. 1 (dashed line). In order to minimize potential errors resulting from this procedure, we also directly measured viscosity within

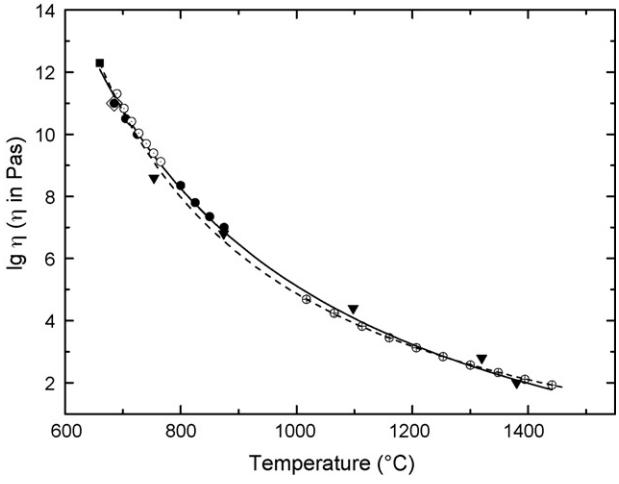

Fig. 1. Glass viscosity vs. temperature obtained from different methods. Solid square: T_g (horizontal dilatometer), open circles: bending beam, solid spheres: parallel plate (force controlled), open diamond: parallel plate (path controlled), solid triangles: heating microscope, crossed open spheres: concentric cylinder viscometry. Fits of Vogel–Fulcher–Tamann equation: solid curve – all data ($A = -4.27$, $B = 7487\,^{\circ}$C, $C = 202\,^{\circ}$C) and dashed curve – T_g and rotational viscometry only.

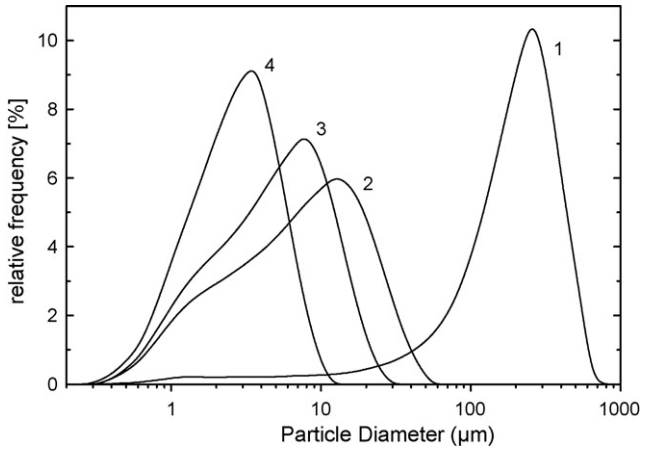

Fig. 2. Particle size distribution of glass (1–3) and GMC (4) powder after different milling steps. 1: jaw crushing, 2: vibration ball milling, 3: attritor milling to $D_{50} = 5$ μm and 4: attritor mix-milling to $D_{50} = 3$ μm.

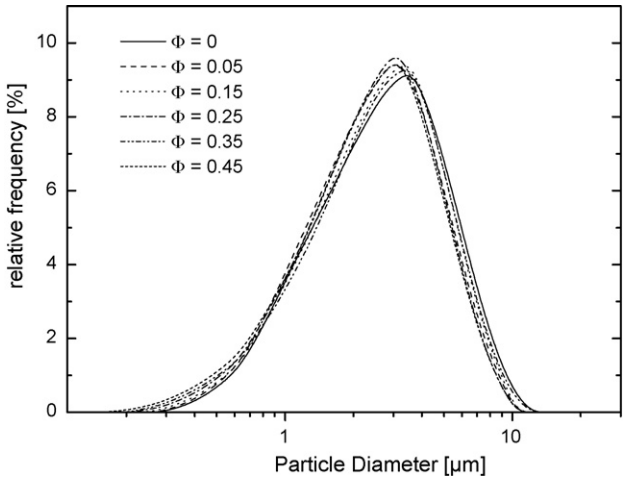

Fig. 3. Particle size distribution of composite powders with alumina particle volume contents $\Phi = 0$–0.45 milled to $D_{50} = 3$ μm. The alumina particle volume content (Al_2O_3) is listed in the legend.

that temperature range by parallel plate viscometry (Fig. 1, solid points). Density at room temperature is $2.707 \pm 0.001\ g\,cm^{-3}$, the coefficient of thermal expansion is $(4.6 \pm 0.25) \times 10^{-6}\ K^{-1}$ and glass transition temperature is 666 °C for thermal cycling at 5 K/min.

3.2. Particle size distribution

The evolution of the PSD shows that the applied milling progress causes an increase of smaller particle size fractions at the expense of coarser fractions (Fig. 2). This way, the broad and asymmetric initial PSD (curve 1) is narrowed and transformed to a more symmetric shape (curve 4). The most frequent particle size and the average particle size, which is common used to characterize ceramic powders, converge to be similar below an average size around 5 μm. We could tune the particle size of GMC powders to almost the same final PSD for Φ from 0 to 0.45 by varying the milling time (Fig. 3).

3.3. Microstructure evolution

Micrographs of polished cross-sections of GMC illustrate the microstructure evolution during sintering for $\Phi = 0.15$, 0.35, and 0.45, respectively (Figs. 4–6). The samples were heated

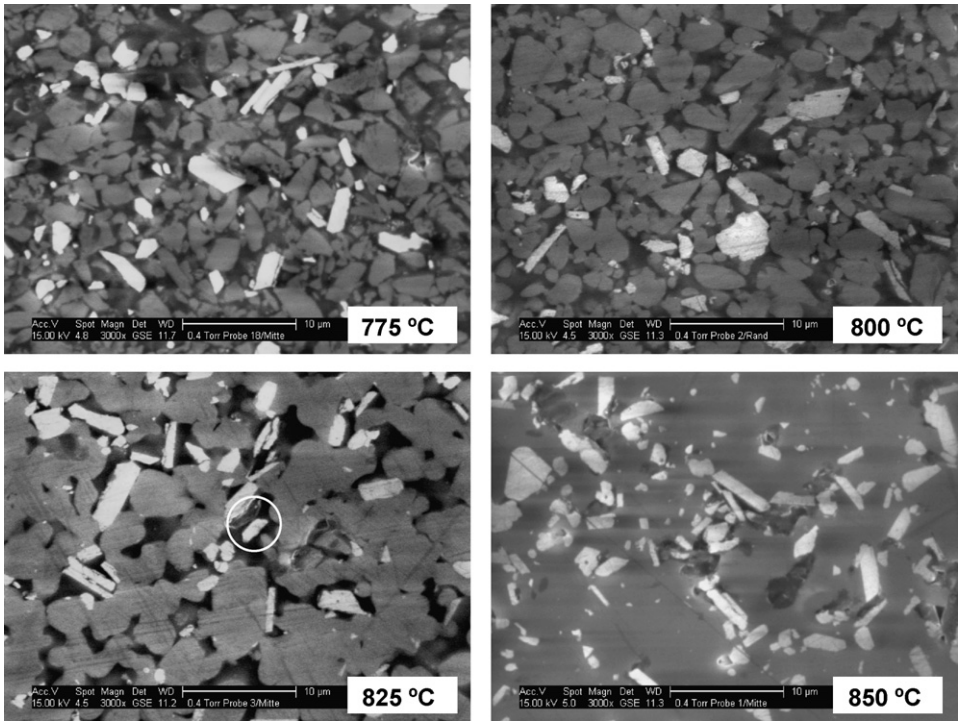

Fig. 4. ESEM-micrographs of polished cross-sections of powder compacts ($\Phi = 0.15$) after heating at 5 K/min to temperatures indicated and subsequent air quenching. Relative density of powder compacts: 61.1% at 775 °C, 66.4% at 800 °C, 80.2% at 825 °C, 93.6% at 850 °C. Bright: Al_2O_3, grey: glass and dark: pores.

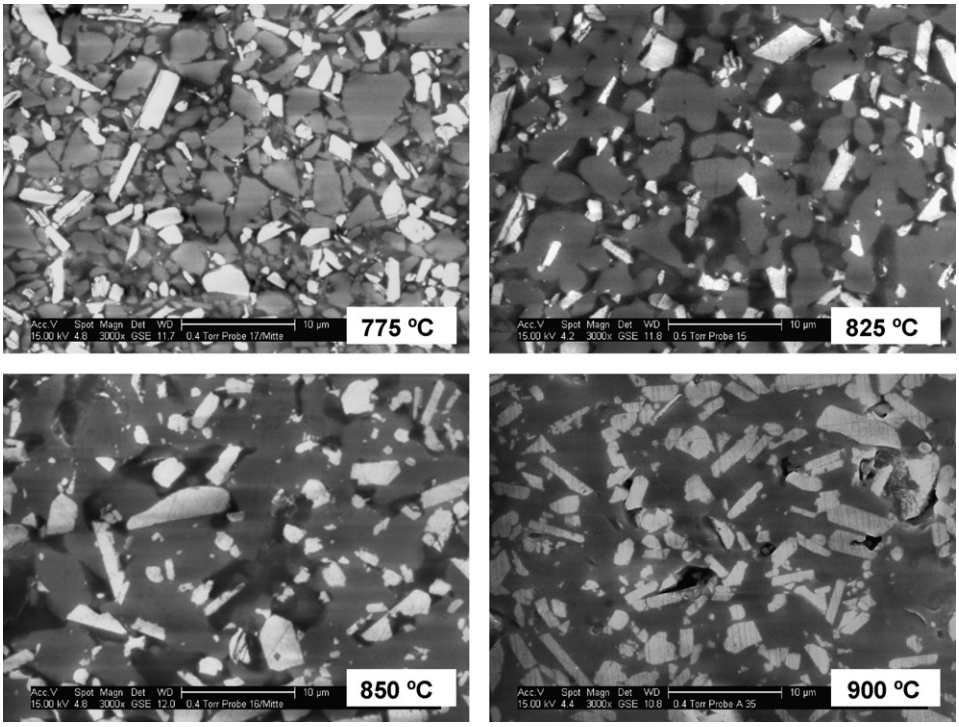

Fig. 5. ESEM-micrographs of polished cross-sections of powder compacts ($\Phi = 0.35$) after heating at 5 K/min to temperatures indicated and subsequent air quenching. Relative density of powder compacts: 60.2% at 775 °C, 70.8% at 825 °C, 80.6% at 850 °C, 91.7% at 900 °C. Bright: Al_2O_3, grey: glass and dark: pores.

at 5 K/min to the temperature indicated and air-quenched immediately.

(i) Images of the microstructures of the early stage (top left micrographs in Figs. 4–6) show that the applied powder processing resulted in equally sized particles of glass (grey) and α-Al_2O_3 particles (white), which confirms the narrow PSD shown in Fig. 3. Despite size similarity, particle shape differs between glass and corundum. A specific number of corundum particles show preferred platelet-like fracturing, while

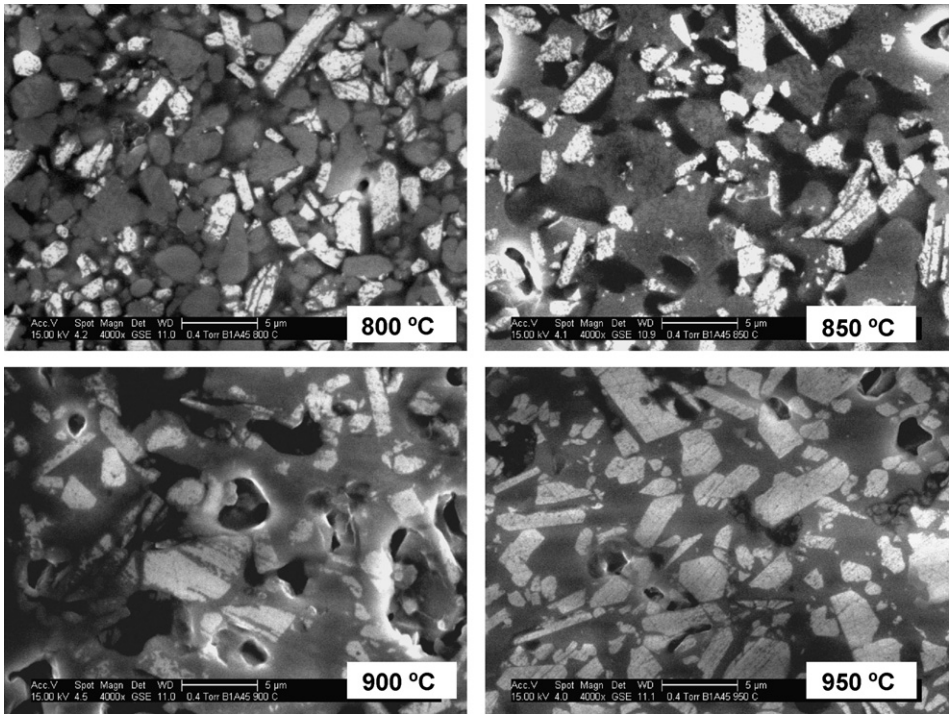

Fig. 6. ESEM-micrographs of polished cross-sections of powder compacts ($\Phi = 0.45$) after heating at 5 K/min to temperatures indicated and subsequent air quenching. Relative density of powder compacts: 59.8% at 800 °C, 68.2% at 850 °C, 78.6% at 900 °C, 85.0% at 950 °C. Bright: Al_2O_3, grey: glass and dark: pores.

milled glass grains exhibit mostly triangular or more complex shapes of dominating intersections. Some corundum platelets seem to have remained in neighbored positions and form closely packed stacks, which do not bear essential cavity. Treating these stacks as one particle, most corundum particles are fully surrounded by glass indicating good mixing, at least on a scale above the mean particle size.

(ii) Intermediate stages of sintering include first particle contacts (upper right and lower left micrographs in Figs. 4–6), e.g. at 775 °C ($\Phi = 0.15$), where the glass viscosity η is $\approx 10^9$ Pa s and particles are sharp edged. At 800 °C ($\eta \approx 10^{8.2}$ Pa s), glass particles are slightly rounded and form more sintering contacts. The cross-section at 825 °C indicates the occurrence of closed porosity. At this temperature, were glass viscosity is about $10^{7.7}$ Pa s (Fig. 1), glass particles are fully rounded, forming dense large agglomerates as well as a thoroughly connected matrix.

Micrographs of intermediate stages in Figs. 4–6 also allow observing corundum–glass contact angles. Although the pictures do not allow a quantitative evaluation, the angles seem to scatter roughly around 90°. This indicates similar energies at the crystal/pore and crystal/liquid interfaces. At least, the observed contact angles may explain why the kinetics of sintering of the GMC under study at 5 K/min could be modeled neglecting the contribution of the crystal/pore and crystal/liquid interfacial energy.[49] We are aware, however, that the kinetics of wetting can intricately depend on time and temperature.[28]

Intermediate stages of microstructural evolution are further characterized by progressive wetting of corundum particles. To quantify this effect we introduce the wetted fraction f of the corundum particle surface area. f was obtained from the cross-sections by means of image analysis. Results are presented in Fig. 7 for $\Phi = 0.15$ (solid spheres) and 0.35 (open spheres). In order to avoid errors caused by spatial density fluctuations, f and the local relative density, ρ, were determined from the same micrograph. Nevertheless, large data scatter is evident. The accuracy of porosity measurement is affected by depth of focus and changes in contrast of used ESEM micrographs resulting in an inaccuracy of ρ of up to ± 0.1.

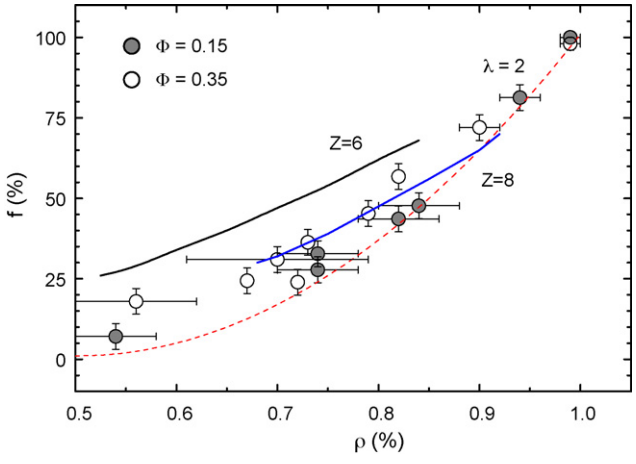

Fig. 7. Wetted fraction f of corundum particles vs. relative density ρ. Dashed curve: according to Eq. (1) with $\lambda = 2$ and $\rho_0 = 0.5$; solid curves according to 0 for different coordination ($Z = 6$ and $Z = 8$).

f is about 0 at the initial stage of sintering where the relative density, ρ, still equals the green density, ρ_0. With increasing ρ, f approaches ≈ 1 for $\rho \approx 1$ at the final state of sintering. Between these limits f steadily increases. The ρ-dependence of the wetted fraction f can be described phenomenologically by Eq. (1) (dashed line in Fig. 7):

$$f = \left[\frac{\rho - \rho_0}{1 - \rho_0}\right]^{\lambda} \quad (1)$$

The solid lines refer to,[50] who calculated the equilibrium contact area for a powder compact of spheres for different coordination numbers, Z. It is reasonable, that the measured f data fall below this prediction: first, initial particle rearrangement may yield an increase of Z ($Z = 6$ simple cubic lattice corresponding to a green density of $\rho_0 = 0.52$, and $Z = 8$ b.c.c. lattice with $\rho_0 = 0.68$), and second,[50] does not take into account the presence of rigid inclusions.

Progressive wetting of corundum particles during sintering could influence the effective viscosity of the powder compact. Corundum particles, which are almost non-wetted (circles in Fig. 4, 825 °C) or those surrounded by other corundum particles cannot fully interact with the viscous matrix and should therefore not increase the effective viscosity of the composite to the extent known from non-porous disperse systems.[51] With continued wetting of the Al_2O_3 particles progressive increase of the effective viscosity should be to expect.

(iii) The final stage of sintering is reached at 850 °C ($\eta \approx 10^{7.2}$ Pa s). Quite similar microstructure evolution was observed for $\Phi = 0.35$ (Fig. 5) and $\Phi = 0.45$ (Fig. 6). One may note that the glass particle or pore shape is identical for a given temperature independent of Φ. Corresponding stages of densification, however, are shifted to higher temperature and glass viscosity and the end of shrinkage is attained at 925 and 1050 °C, respectively (see Fig. 12). This means that the force for local material transport by viscous flow remains the same but macroscopic flow conditions are changed by the presence of rigid inclusions.

The final stage of sintering (bottom right micrographs in Figs. 4–6) most strikingly indicates the occurrence of 3- or 4-particle corundum clusters bearing remaining pores. Increased alumina particle volume content Φ leads to more frequent occurrence of such Al_2O_3 clusters. Nevertheless, this effect may be partially reduced by the related lower glass viscosity or better wetting at the extended temperature range of final densification.

3.4. Shrinkage

Initially, the influence of load on the axial shrinkage of glass powder compacts ($D_{50} = 5$ μm) was investigated using heating microscopy (load free), vertical dilatometry (sintering pressure was 0.2 and 0.6 kPa) and horizontal dilatometry data (sintering pressure was 1.6 kPa) (Fig. 8). Additional to the axial shrinkage,

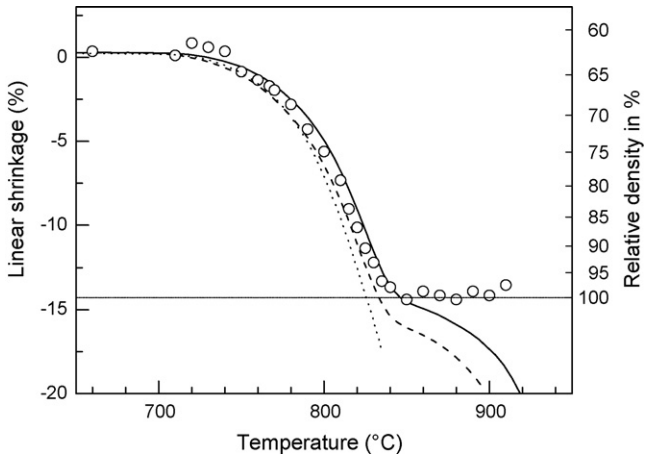

Fig. 8. Axial shrinkage, s, of glass powder compacts ($D_{50} = 5\,\mu m$) during heating at 5 K/min. Open circles: heating microscope (pressure free), solid line: vertical dilatometer (1 cN = 0.2 kPa), dashed line: vertical dilatometer (3 cN = 0.6 kPa) and dotted line: horizontal dilatometer (4 cN = 1.6 kPa). The right ordinate presents the relative density, ρ, calculated from the linear shrinkage shown by the left ordinate and a compact green density of 63% according to Eq. (1).

s, we also present in Fig. 8 the relative density ρ, which is given for isotropic sintering according to[14]

$$s(t) = 1 - \left(\frac{\rho_0}{\rho[t]}\right)^{1/3} \quad (2)$$

With increasing load, the axial shrinkage rate increases. Furthermore, the load-induced axial flow strongly affects the final stage of sintering. Thus, maximum linear shrinkage of about 14% was measured by means of load free heating microscopy which correlates to the value expected from Eq. (2) for $\rho_0 = 0.63$. For a sintering pressure of 0.2 kPa, the axial shrinkage obtained by vertical dilatometry is about the same size as $s(t)$ from heating microscopy, especially in the onset range and the range of maximum densification velocity. One may estimate the temperature of final shrinkage from the inflexion point of the $s(t)$ curve (Fig. 8). In the range of final densification, however, ≈17% maximum shrinkage is evident, which pretends $\rho > 100\%$ in terms of Eq. (2). For increasing loading (0.6 and 1.6 kPa) the final stage of shrinkage could not be detected from the shrinkage curve.

The sintering of the GMC under study ($D_{50} = 3\,\mu m$; $\Phi = 0$–0.45, Fig. 9) shows a similar trend. Thus, the temperature, e.g. at which a shrinkage of 12% is attained, decreases by ≈20 K with increasing load (Fig. 9, $\Phi = 0$) and, for each Φ, the highest mean densification rate is evident for horizontal dilatometer measurements (1.6 kPa). The axial shrinkage is obviously affected by load-induced creep as most easily seen at the final stage of shrinkage. The intensity of this creep reduces with increasing Φ. The shrinkage detected by the vertical dilatometer (0.2 kPa) shows good agreement with axial heating microscope data. Although the temperature of minimal vertical dilatometer shrinkage rate of can be used as a rough estimate of the temperature of maximum axial shrinkage, no saturation of shrinkage is actually detectable with this method.

Hence, load free shrinkage measured by heating microscopy is essential for kinetic modeling of shrinkage. These data, how-

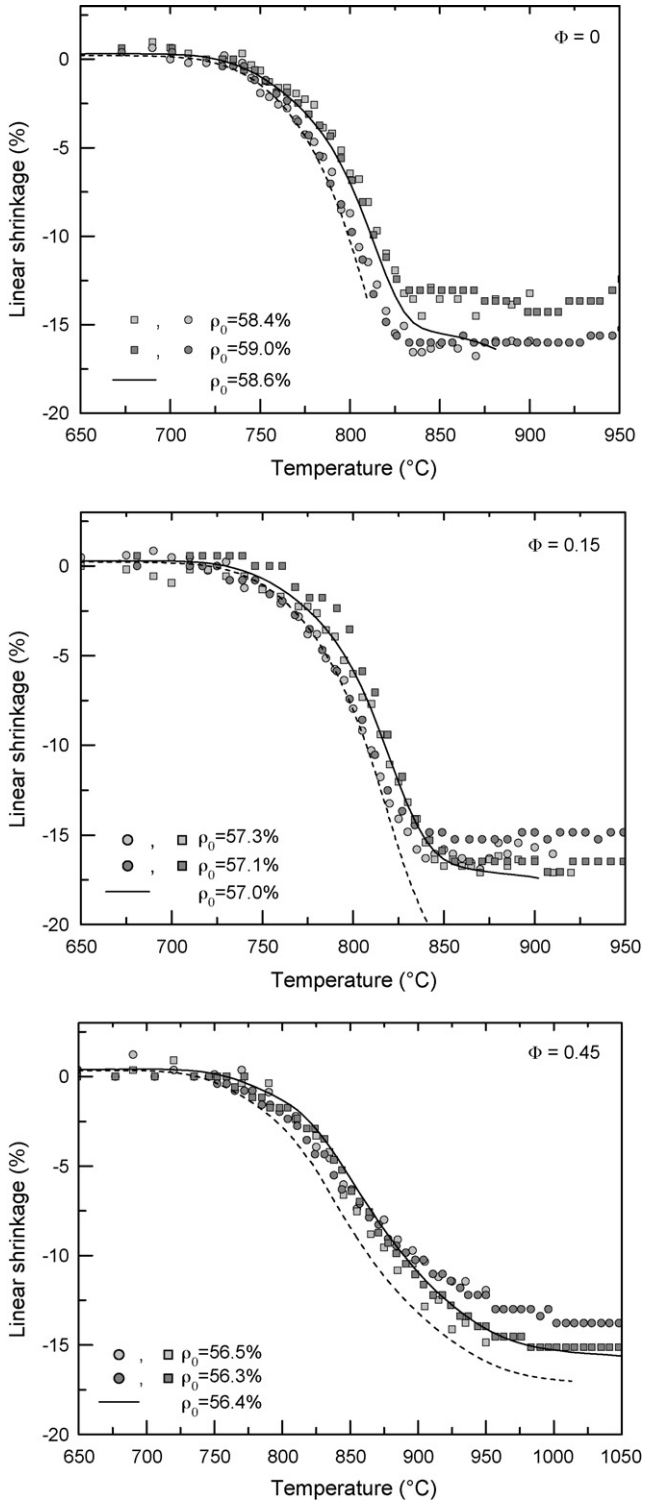

Fig. 9. Linear shrinkage vs. temperature of composite powder compacts ($\Phi = 0$, 0.15, 0.45) during heating at 5 K/min. Spheres: heating microscopy radial shrinkage (pressure free), squares: heating microscopy axial shrinkage (pressure free) and light grey: Berlin. Dark grey: Clausthal. Solid line: vertical dilatometer (1 cN = 0.2 kPa), dashed line: horizontal dilatometer (4 cN = 1.6 kPa). Green density ρ_0 see legend.

ever, reveal systematic differences between radial and axial strain. Thus, radial shrinkage tends to start earlier, at least for $\Phi < 0.45$ (Fig. 9). This trend, however, is compensated by an increased axial to radial shrinkage rate ratio with increasing Φ. As a result, there is a systematic trend concerning the attainable maximum axial and radial shrinkage. The maximum radial shrinkage of the composites $\Phi = 0$–0.05 (not shown) is higher than the maximum axial shrinkage. By contrast, the maximum radial shrinkage of the composites $\Phi = 0.15$–0.45 is less than the maximum axial shrinkage. Note that this result is confirmed by two different heating microscopes (circles and cubes by Fig. 9).

3.5. Dissolution

Sintering of the GMC under study can be influenced by dissolution of the corundum particles into the glass. Since such a dissolution will decrease Φ, we applied image analysis (software Image C) to polished cross-sections of sintered composites with $\Phi = 0.35$ in order to measure the alumina volume fraction after sintering. Eventual dissolution during sintering should be easy observable since the initial alumina volume fraction was chosen to be rather high and the whole temperature range of LTCC sintering was covered. Measured Φ, however, was 0.36 (image analysis, no standard deviation) after heating at 5 K/min to 900 °C, which is very close to the initial value of 0.35. Accordingly, dissolution of corundum particles, under these firing conditions is lower than 1 vol.% and was regarded as negligible.

3.6. Glass crystallization

Sintering of GMC can be further influenced by simultaneous crystallization.[16] Crystallization should be best detectable in composites containing high amounts of corundum particles ($\Phi = 0.35$ and 0.45). DTA curves of glass powder compacts as well as of composites with $\Phi = 0.15$ and 0.45 show no crystallization peaks (Fig. 10). Therefore, crystallization was considered to be negligible. Additionally, dense sintered specimens of powder compacts with $\Phi = 0.35$ and 0.45 (sintered for 20 min at 850 and 950 °C, respectively) were grinded to a flat shape and subjected to XRD. The composite with $\Phi = 0.35$ shows corundum peaks only (Fig. 11, top). The XRD patterns for $\Phi = 0.45$ (Fig. 11, bottom) shows additionally weak peaks indicating minor amounts of $BaAl_2Si_2O_8$, but near to the detection limit.

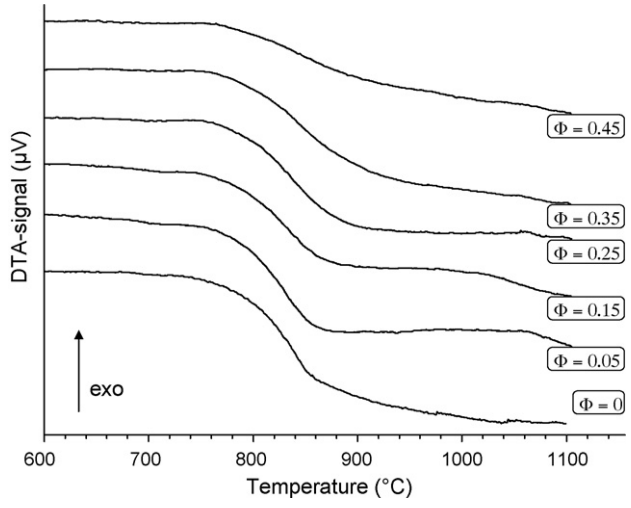

Fig. 10. Thermal analysis (DTA) of composite powder compacts $\Phi = 0$–0.45. The week endothermal step around 800 °C indicates a change of heat capacity due to decreasing porosity during sintering.

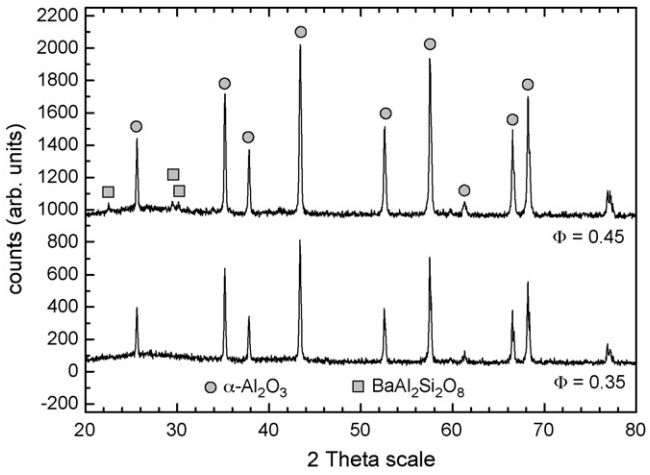

Fig. 11. X-ray pattern (XRD) of composite powder compacts $\Phi = 0.35$ and $\Phi = 0.45$ isothermally (20 min) sintered to maximum density at 850 and 950 °C, respectively. The pattern of $\Phi = 0.35$ contains corundum peaks of the regular 0.35-fraction only. The pattern of $\Phi = 0.45$ additionally contains peaks of $Ba_2Al_2SiO_8$ close to the detection limit of 2–5% by mass.

4. Discussion

4.1. Shrinkage data correction

Any discussion of shrinkage data, e.g. kinetic modeling of shrinkage, is limited by the experimental accuracy. Using heating microscopy, one can minimize falsifying effects of load on sintering experiments. These data, however, still includes systematic differences between radial and axial shrinkage (Fig. 9). Non-isotropic features of the specimen's green body microstructure may explain that radial shrinkage starts earlier.[15] Although no orientation might be to appear at a first glance in the micrographs of polished cross-sections, the radial packing might be somewhat lower than the axial packing caused by non-spherical particles and uniaxial pressing. The initial sintering force is then higher in radial direction. With increasing Φ, this effect is overlapped by progressively accelerated axial shrinkage. These phenomena are not understood so far.

Anisotropy effects discussed above can falsify linear shrinkage by up to 5%. These data is therefore not appropriate for the discussion of the effect of Φ on the shrinkage behaviour of LTCC GMC. To overcome this, we calculated volume shrinkage from axial and radial heating microscopy data (Clausthal measurements, dark grey points in Fig. 9). This volume shrinkage was recalculated to the linear shrinkage, which is to expect for isotropic sintering. In order to account for the scatter in green density within the sample set, this linear isotropic shrinkage was

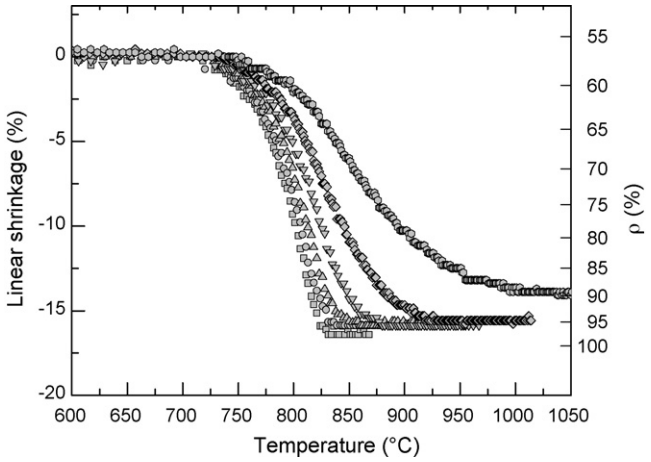

Fig. 12. Linear shrinkage vs. temperature of composite powder compacts ($\Phi = 0$–0.45) during heating at 5 K/min. Corrected heating microscopy data. Squares: $\Phi = 0$, spheres: $\Phi = 0.05$, up triangles: $\Phi = 0.15$, down triangles: $\Phi = 0.25$, diamonds: $\Phi = 0.35$ and hexagons: $\Phi = 0.45$. The right ordinate presents the relative density, which was calculated from the linear shrinkage shown by the left ordinate and a compact green density of 57%.

then corrected with respect to the mean green density of 57% by constant factors reflecting the different attainable isotropic shrinkage s_i for different green density according to Eq. (1). Suchwise corrected linear shrinkage data are shown in Fig. 12.

4.2. Effect of small rigid inclusion on shrinkage

The effects of small rigid inclusions are discussed here in terms of corrected linear shrinkage (Fig. 13). The composites $\Phi < 0.15$ show very small effects on strain as well as no essential reduction of attainable shrinkage. For $\Phi > 0.15$ the shrinkage rate starts to decrease significantly during later stages. By contrast, the early stage of sintering is much less influenced. For example, the early stage shifts for $\Phi = 0.45$ around 20 K to higher temperature. During the intermediate stages the shrinkage rate is progressively lowered. The temperature of the final stage of shrinkage of $\Phi = 0.45$ shifts by up to 170 K. In general, the inflexion point of shrinkage vs. temperature curve shifts to higher temperatures whereas the onset temperature of sintering remains at the same level resulting in rather concave strain curves with increasing Φ. These observations indicate, that Φ has a complex influence on the effective GMC viscosity. Related studies have been made for the present system and will be reported in a separate paper.

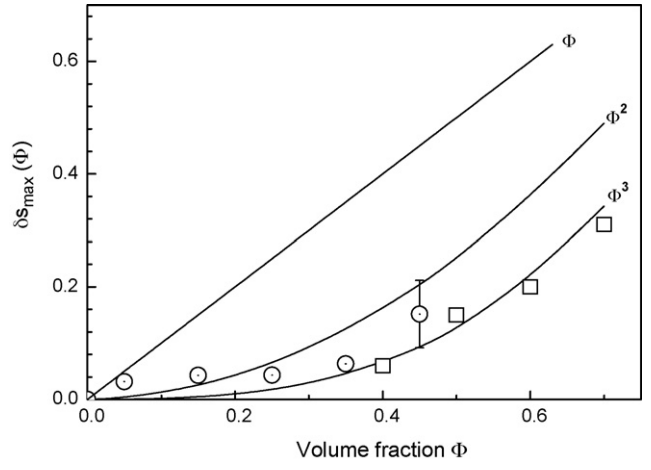

Fig. 13. Reduced maximal shrinkage δs^{max} vs. Φ of composite powder compacts according to Eq. (2). Spheres: this work (data taken from Fig. 12). Squares: calculated from GMC sintering data reported by Jean and Gupta 0.

Despite its marked influence on strain rate, $\Phi > 0.15$ also reduces the attainable total shrinkage. The latter effect can be quantified by the reduced maximal shrinkage, $\delta s^{max}(\Phi)$

$$\delta s^{max}(\Phi) = 1 - \frac{s^{max}(\Phi)}{s_0^{max}} \tag{3}$$

where $s^{max}(\Phi)$ is the maximum shrinkage of the GMC and s_0^{max} the maximum shrinkage of glass powder compacts. δs^{max} obtained from Fig. 12 is shown in Fig. 13 vs. Φ (open spheres). The error bar indicates the average deviation of δs^{max} obtained in two independent series of sintering experiments. The open squares were calculated from shrinkage data reported in Ref. [28] for Cordierite crystals dispersed in borosilicate glass. The microstructure reported there is similar to the present case. It is interesting to note that, despite some scatter, δs^{max} is roughly proportional to Φ^3. The reduced densification, which was attributed to residual pores stabilized by corundum cluster (see Figs. 4–6), supports the dependence of δs^{max} on Φ^3.

4.3. Mixing and wetting

The proportionality $\delta s^{max} \sim \Phi^3$ observed in Fig. 13 can be expected when (i) three-particle corundum clusters, which occur with a probability of Φ^3 for ideal mixing and (ii) form rigid central pores. In fact, three-particle corundum clusters bearing residual pores are evident from the electron micrographs (Figs. 4–6). Further, this images show good mixing. Good mixing can also be anticipated for LTCC systems fabricated in an industrial process. The formation of residual pores by three-particle clusters, however, must not be treated as a general rule for LTCC. In the present case, this behaviour could be related to the platelet-like shape of corundum particles, which can form cavities more easily than, e.g. spheres. For better-rounded corundum particles, more than 3 neighbored particles may be required to form a remaining cavity and $\delta s^{max} \sim \Phi^n$ with $n > 3$ could appear.

On the other hand, n should depend on the glass–corundum contact angle θ. If θ is slightly above 90°, even spaces formed by parallel walls will be not wetted. If θ decreases with increasing temperature as indicated by previous studies[28–32] $\delta\sigma^{max}$ could increase, e.g. with Φ^2 for small Φ, i.e. for low-temperature range of sintering, whereas a Φ^3 may dominate else. Such trend might even be inferred from Fig. 13.

For other wetting behaviour, particle shapes and size relation, the dependence of $\delta\sigma^{max}$ upon Φ may differ.[52,53]

Another effect which could limit the densification is a partial local dissolution of Al_2O_3 into the glass phase. Although we did not find indications pointing to that, liquid phase volumes next to Al_2O_3 particle surfaces may undergo a limited alumina enrichment, which will be enhanced in surroundings of particle

clusters and at elevated temperatures. In this case, the flow of the alumina enriched liquid phase into particle clusters can be hindered by increased viscosity.

In general, such behaviour can be quite complex and is basically bound between two limiting cases. As the upper bound, δs^{max} should be proportional to Φ if bad mixing causes complete agglomeration of dispersed crystal particles and strong non-wetting behaviour and/or a viscosity increase prevents the glass from penetrating the agglomerates. In this case, the crystal particles fix porosity proportional to Φ (straight line in Fig. 13). As the lower bound, δs^{max} is expected to stay zero for spreading and/or an unchanged or lowered viscosity. In any case, the measure of $\delta s^{max}(\Phi)$ and its discussion based on microstructure analysis data is quite important to ensure sinter kinetic understanding and modeling.

5. Conclusions

We studied sintering of glass matrix composites (GMC) for LTCC applications, which are typically obtained from glass and crystal powders of similar and small average particle size ($D_{50} \approx 3\,\mu m$). To reveal the effect of such small rigid inclusions on sintering, we studied a non-reactive GMC obtained from up to 45 vol.% Al_2O_3 ($\Phi = 0.45$) and alumo-borosilicate glass powders, which do not show detectable chemical solution of crystal particles into the glass and crystallization during the time-temperature scale of LTCC sintering as checked by DTA and XPD measurements.

Glass viscosity was measured by complementary methods. All measured data well fit the VFT-equation $\log(\eta/\mathrm{Pa\,s}) = A + B/(T - C)$ with $A = -4.27$, $B = 7484\,^{\circ}C$ and $C = 202\,^{\circ}C$ within 0.2 log units accuracy. Microstructure analysis confirms good powder mixing and a small and similar particle size as measured by laser scattering methods. Al_2O_3 particle clusters bearing residual pores become more frequent with increasing Φ. For the temperature range of sintering, medium wetting is indicated by the glass/Al_2O_3 contact angle θ, which roughly scatters around 90°.

Shrinkage was measured from uniaxially pressed powder compacts by dilatometry and heating microscopy. Even for the small sintering loads applied, dilatometer shrinkage data were falsified by load-induced viscous flow. Thus, heating microscopy turned out best appropriate despite non-isotropy of sintering even there. In order to account for this effect and for scatter in green density, an isotropic linear shrinkage was calculated from axial and radial shrinkage data. This shrinkage was then corrected by a constant factor reflecting the different attainable isotropic shrinkage for different green density. Thus corrected isotropic shrinkage data showed that increasing dispersed crystalline particle volume content Φ has decelerating influence on sintering. Whereas this effect is small for $\Phi \leq 0.15$, the end of shrinkage shifts to higher temperatures by up to 170 K for $\Phi = 0.45$. Furthermore, the attainable shrinkage progressively reduces with increasing Φ as residual pores enveloped by at least three Al_2O_3 particles become more frequent. The reduce roughly increases with Φ^3, reaching about 8% for $\Phi = 0.45$.

Although many features of the model system under study are typical for LTCC applications, the presented results are restricted to the given shape of corundum particles, degree of mixing, wetting and chemical interaction between the dispersed rigid particles and the glass matrix. Further studies are required with respect to chemical solution during sintering and its consequences on the glass viscosity, the wetting behaviour and the effective viscosity of GMC.

Acknowledgements

Financial support of the Deutsche Forschungsgemeinschaft (DFG) under grants De 598/7, and Mu 963/7 is gratefully acknowledged. The authors thank J. Biberstein, M. Buchholz, W. Güther, T. Moelders, R. Schadrack (BAM), and H. Bornhöft (TU Clausthal) for measurements and sample preparation.

References

1. Tummala, R. R., Ceramic and glass–ceramic packaging in the 1990s. *J. Am. Ceram. Soc.*, 1991, **74**, 895–908.
2. Wilcox, D. L. and Oliver, M., LTCC, an interconnect technology morphing into a strategic microsystem integration technology. In *Proceedings of Advanced Technology Workshop on Ceramic Applications for Microwave and Photonic Packaging. Providence*. IMAPS—International Microelectronics and Packaging Society, Rhode Island, 2002.
3. Rabinovich, E. M., Review preparation of glass by sintering. *J. Mater. Sci.*, 1985, **20**, 4259–4429.
4. Frenkel, J., Viscous flow of crystalline bodies under the action of surface tension. *J. Phys. Moscow*, 1945, **9**, 385–391.
5. Mackenzie, J. K. and Shuttleworth, R., Phenomenological theory of sintering. *Proc. Phys. Soc. Lond.*, 1949, **62**, 833–852.
6. Exner, H. E. and Giess, E. A., A stereology based equation for isotropic shrinkage during sintering by viscous flow. In *Proceedings of Seventh World Round Table Conference on Sintering. Herceg-Novi, Yugoslavia*. Plenum Press, New York, 1990.
7. Olevsky, E. A., Theory of sintering: from discrete to continuum. *Mater. Sci. Eng. R: Rep.*, 1998, **23**, 41–100.
8. Scherer, G. W., Sintering of low-density glass. I. Theory. *J. Am. Ceram. Soc.*, 1977, **60**, 236–239.
9. Lange, F. F., Sinterability of agglomerated powders. *J. Am. Ceram. Soc.*, 1984, **67**, 83–89.
10. Clasen, R., Sintering behaviour of submicron silica particles. *Glastech. Ber.*, 1989, **62**, 234–243.
11. Scherer, G. W., Cell models for viscous sintering. *J. Am. Ceram. Soc.*, 1991, **74**, 1523–1531.
12. Scherer, G. W., Viscous sintering of a bimodal pore–size distribution. *J. Am. Ceram. Soc.*, 1984, **67**, 709–715.
13. Prado, M. O., Zanotto, E. D. and Mueller, R., Model for sintering polydispersed glass particles. *J. Non-Cryst. Solids*, 2001, **279**, 169–178.
14. Exner, H. E. and Giess, E. A., Anisotropic shrinkage of cordierite-type glass powder cylidrical compacts. *J. Mater. Res.*, 1988, **3**, 122–125.
15. Boccaccini, A. and Ondracek, G., Viscous sintering of non-spherical borosilicate-glass powder. *Glass Sci. Technol.*, 1992, **65**, 73–78.
16. Zanotto, E. D. and Prado, M. O., Isothermal sintering with concurrent crystallisation of monodispersed and polydispersed glass particles. Part 1. *Phys. Chem. Glasses*, 2001, **42**, 191–198.
17. Boccaccini, A., Bücker, M. and Bossert, J., Glass and glass-ceramics from coal fly-ash and waste glass. *Tile Brick Int.*, 1996, **12**, 515–518.
18. Blendell, J. E., Locatelli, M. R., Wallace, J. S. and Hockey, B. J., Modelling of anisotropic shrinkage during sintering of low temperature co-fired ceramic tapes. In *Proceedings of Advanced Technology Workshop on Ceramic Applications for Microwave and Photonic Packaging*. IMAPS-International Microelectronics And Packaging Society, Providence, Hode Island, 2002.

19. Ferraris, M. and Verne, E., Viscous phase sintering of particle-reinforced class matrix composites. *J. Eur. Ceram. Soc.*, 1996, **16**, 421–427.
20. Boccaccini, A., Investigation of the sintering of composite glass powder compacts using heating microscopy. *Fund. Glass Sci. Technol.*, 1997.
21. Rozenstrauha, I., Cimdins, R., Berzina, L., Bajare, D. and Bossert, J., Sintered glass–ceramic matrix composites made from Latvian silicate wastes. *Glass Sci. Technol.*, 2002, **75**, 132–139.
22. Eberstein, M., Schiller, W. A., Dernovsek, O. and Wersing, W., Adjustment of dielectric properties of glass ceramic composites via crystallization. In *Proceedings of the International Symposium on Crystallization in Glasses and Liquids Proceedings*. Verlag der Deutschen Glastechnischen Gesellschaft, Vaduz, 2000, pp. 371–373.
23. Boccaccini, A., Kim, K. D. and Ondracek, G., Zur Viskosität von Glasschmelzen und porösen Sintergläsern. *Mat. -wiss. u. Werkstofftech.*, 1995, **26**, 263–268.
24. Boccaccini, A. and Olevski, E. A., Processing of platelet-reinforced glass matrix composites: effect of inclusions on sintering anisotropy. *J. Mater. Process. Technol.*, 1999, **96**, 92–101.
25. Scherer, G. W., Sintering with rigid inclusions. *J. Am. Ceram. Soc.*, 1987, **70**, 719–725.
26. Lange, F. F., Constrained network model for predicting densification behaviour of composite powders. *J. Mater. Res.*, 1987, **2**, 59–65.
27. Jonghe, L. C. D. and Rahaman, M. N., Sintering stress of homogeneous and heterogeneous powder compacts. *Acta Metall.*, 1988, **36**, 223–229.
28. Jean, J.-H. and Gupta, T. K., Densification kinetics of the initial stage of liquid phase sintering: glass–cordierite system. *J. Mater. Sci. Lett.*, 1992, **11**, 656.
29. Huang, T. S., Rahaman, M. N., Elred, B. T. and Ownby, P. D., Wetting of mullite by Y_2O_3–Al_2O_3–SiO_2 and B_2O_3–SiO_2 glasses. *J. Mater. Res.*, 2001, **16**, 3223–3228.
30. Weirauch Jr., D. A., Lazaroff, J. E. and Ownby, P. D., Wetting in an electronic packaging ceramic system. II. Wetting of alumina by a silicate glass melt under controlled p_{O_2} conditions. *J. Am. Ceram. Soc.*, 1995, **78**, 2923–2928.
31. Weirauch Jr., D. A. and Ziegler, D. P., Surface tension of aluminosilicate glass using computerized drop shape analysis. *J. Am. Ceram. Soc.*, 1996, **79**, 920–926.
32. Kuromitsu, Y., Yoshida, H., Takebe, H. and Morinaga, K., Interaction between alumina and binary glasses. *J. Am. Ceram. Soc.*, 1997, **80**, 1583–1587.
33. Ollagnier, J.-P., Guillon, O. and Rödel, J., Viscosity of LTCC determined by discontinuous sinter-forging. *Int. J. Appl. Ceram. Technol.*, 2006, **3**, 437–441.
34. Ollagnier, J.-P., Guillon, O. and Rödel, J., Effect of anisotropic microstructure on the viscous properties of an LTCC material. *J. Am. Ceram. Soc.*, 2007, **90**, 1–6.
35. Mohanram, A., Messing, G. L. and Green, D. J., Densification and sintering viscosity of low-temperature co-fired ceramics. *J. Am. Ceram. Soc.*, 2005, **88**, 2681–2689.
36. Mohanram, A., Lee, S.-H., Messing, G. L. and Green, D. J., Constrained sintering of low-temperature co-fired ceramics. *J. Am. Ceram. Soc.*, 2006, **89**, 1923–1929.
37. Christensen, R. M., *Theory of Viscoelasticity. An Introduction* (*2nd ed.*). Academic Press, New York, 1982.
38. Scherer, G. W. and Rekhson, S. M., Viscoelastic-elastic composites. I. General theory. *J. Am. Ceram. Soc.*, 1982, **65**, 352–360.
39. Venkatachari, K. and Raj, R., Shear deformation and densification of powder compacts. *J. Am. Ceram. Soc.*, 1986, **69**, 499–506.
40. Raj, R., Analysis of the sintering pressure. *J. Am. Ceram. Soc.*, 1987, C-210–C211.
41. Bordia, R. K. and Scherer, G. W., Overview No. 70, On constrained sintering. I. Constitutive model for a sintering body. *Acta Metall.*, 1988, 2393–2397.
42. Bordia, R. K. and Scherer, G. W., Overview No. 70, On constrained Sintering. II. Comparison of constitutive Models. *Acta Metall.*, 1988, 2399–2409.
43. Bordia, R. K. and Scherer, G. W., Overview No. 70, On constrained sintering. III. Rigid inclusions. *Acta Metall.*, 1988, 2411–2416.
44. Scherer, G. W. and Brook, R. J., Creep and densification during sintering of glass powder compacts. *J. Am. Ceram. Soc.*, 1987, **70**, 766–774.
45. Wonisch, A., Guillon, O., Kraft, T., Moseler, M., Riedel, H. and Rödel, J., Stress-induced anisotropy of sintering alumina: discrete element modeling and experiments. *Acta Mater.*, 2007, **55**, 5187–5199.
46. Olevsky, E. A., Tikare, V. and Garino, T., Multi-scale study of sintering: a review. *J. Am. Ceram. Soc.*, 2006, **89**, 1914–1922.
47. German, R. M., *Sintering Theory and Practice*. John Wiley & Sons, New York, 1996.
48. Kingery, W. D. and Narasimhan, M. D., Densification during sintering in the presence of a liquid phase. II. Experimental. *J. Appl. Phys.*, 1959, **30**, 301–310.
49. Müller, R., Eberstein, M., Reinsch, S. and Schiller, W. A., Effect of rigid inclusions on sintering of low temperature co-fired ceramics. *Phys. Chem. Glasses: Eur. J. Glass Sci. Technol. B*, 2007, **48**, 259–266.
50. Svoboda, J., Riedel, H. and Zipse, H., Equilibrium pore surfaces, sintering stresses and constitutive equations for the intermediate and late stages of sintering. I. Computation of equilibrium surfaces. *Acta Metall. Mater.*, 1994, **42**, 435–443.
51. Roscoe, R., Suspensions. In *Flow Properties of Disperse Systems*, J. J. Hermans. ed. North Holland, Amsterdam, 1953, pp. 1–38.
52. Pascual, M. J., Duran, A., Prado, M. O. and Zanotto, E. D., Model for sintering devitrifying glass particles with embedded rigid fibers. *J. Am. Ceram. Soc.*, 2005, **88**, 1427–1434.
53. Kemethmueller, S., Hagymasi, M., Stiegelschmitt, A. and Roosen, A., Viscous flow as the driving force for the densification of low temperature co-fired ceramics. *J. Am. Ceram. Soc.*, 2007, **90**, 64–70.